IEEE Access
Multidisciplinary | Rapid Review | Open Access Journal

Received June 30, 2019, accepted August 2, 2019, date of publication August 9, 2019, date of current version August 22, 2019.

Digital Object Identifier 10.1109/ACCESS.2019.2934224

Non-Data-Aided Cycle Slip Self-Correcting Carrier Phase Estimation for QPSK Modulation Format of Coherent Wireless Optical Communication System

YE WANG[1,2], ZHIYONG WU[1], XUELIANG LI[1], TIANWEN GENG[1], SHUANG MA[1], LIN LI[1,2], SHIJIE GAO[1], AND YATIAN LI[1,2]

[1]Changchun Institute of Optics, Fine Mechanics and Physics, Chinese Academy of Sciences, Changchun 130033, China
[2]University of Chinese Academy of Sciences, Beijing 100049, China

Corresponding author: Yatian Li (yt_li@ciomp.ac.cn)

This work was supported in part by the National Natural Science Foundation of China under Grant 51605465, and in part by the Research Project of Scientific Research Equipment of Chinese Academy of Sciences.

ABSTRACT In this study, we propose a non-data-aided algorithm of the cycle slip self-correcting carrier phase estimation (CSSC-CPE) which mitigates the cycle slips caused by blind CPE in the coherent wireless optical communication (WOC) system. The CSSC-CPE uses the output of CPE for cumulative averaging and selects the difference δ between two cumulative average segments as the discriminant parameter. The location and direction of cycle slips are determined by identifying the position and sign of the peak value of δ. The optimal thresholds for cycle slip detection could be derived from the probability density function (PDF) of δ obtained by calculation and deduction. Finally, numerical simulations and indoor experiments are carried out. The results show that CSSC-CPE can effectively eliminate cycle slips under weak turbulence condition. Compared with relative non-data-aided cycle slip correction algorithms, the CSSC-CPE achieves a better performance in suppressing the phase noise generated by atmospheric turbulence and laser linewidth, which enhances the accuracy of the cycle slip identification and lowers the SNR requirement when the cycle slip is not allowed.

INDEX TERMS Coherent detection, cycle slip, free-space optical communication, phase estimation.

I. INTRODUCTION

The coherent WOC system has been extensively studied due to its superiority to the conventional direct detection system in sensitivity and spectral efficiency [1], [2]. Since information transmission mainly relies on the amplitude and the phase of the carrier, phase noise suppression plays a crucial role in the improvement of system performance. Phase noise is chiefly attributed to the wavefront distortion caused by atmospheric turbulence, laser linewidth, additive white Gaussian noise generated by the receivers and residual carrier frequency offset (CFO). With the development of high-speed digital signal processing (DSP), the method of phase estimation and correction utilizing DSP has become the optimal means to suppress phase noise [3]–[6]. Meanwhile, some CPE algorithms have emerged [7]–[9]. The commonly used blind CPE algorithms based on Viterbi-Viterbi phase estimation (VVPE) contain a phase unwrapping (PU) module to solve inherent phase ambiguity. Unfortunately, cycle slips occur accordingly, which do harm to phases of constellation points [10]–[13]. For the quadrature phase-shift keying (QPSK) system, the cycle slip will cause the decision values of the slip symbol and subsequent symbols to deviate from the correct constellation points by integer multiples of $\pi/2$, thereby leading to consecutive estimation errors and serious degradation of the performance of the communication system.

To cope with the problem of cycle slips, numerous studies have been carried out. Currently, three popular methods are summarized, and they are differential encoding/decoding, data-aided cycle slip correction, independent cycle slip

The associate editor coordinating the review of this article and approving it for publication was Zhaoqing Pan.

correction stage without data assistance, respectively. Firstly, differential encoding/decoding converts permanent phase errors into instantaneous ones at the cost of optical SNR [14]. In Ref [15], it has been discovered that the disadvantages produced by differential encoding/decoding can be avoided by turbo differential decoding. Nevertheless, it has to be guaranteed that cycle slip probability should be no more than 10^{-4} in order to ameliorate the error floor. Secondly, the data-aided cycle slip correction realizes phase estimation by estimating a carrier without cycle slips based on the auxiliary data [16], [17]. As a result, there is no need for differential encoding/decoding, which helps to refrain from additional optical SNR penalties. The third method uses a stage paralleling to CPE to assist in correcting the cycle slips that occur during the CPE process [6], [13], [18]. Ref. [18] proposed a novel cycle slip correction algorithm by calculating discriminant parameters, which not merely avoided the shortcomings of additional optical SNR penalty and the auxiliary data, but also further improved the accuracy of cycle slip correction in combination with other two methods, thereby becoming one of the most promising methods to solve cycle slip issues.

Motivated by the third method, we propose a new algorithm CSSC-CPE which can correct cycle slips without the need of either data assistance or differential encoding/decoding in this paper. The CSSC-CPE performs a second cumulative averaging through the results of CPE, and determines the occurrence of the cycle slip by the difference between two average segments. It is worth noting that the short-time subtraction can also reduce the slowly varying laser linewidth noise to a certain extent, and the phase noise caused by atmospheric turbulence can be better suppressed by two times average of the CPE stage and the cycle slip correction stage. These features enable CSSC-CPE to more accurately find where cycle slip occurs. In the simulation, we take into consideration the time-varying statistical characteristics of the log-normal atmospheric turbulence channel, and introduce the cycle slip correction algorithm proposed in Ref. [18] for comparison. The results illustrate that the frequency of the cycle slip will increase with the rise of atmospheric turbulence intensity. Moreover, compared with the one-time sliding average algorithm, the CSSC-CPE can achieve a lower post-correction cycle slip probability, which means that the proposed algorithm has more advantages in the WOC system. The conclusion was subsequently verified by indoor experiments. Besides, the CSSC-CPE can determine cycle slip direction while identifying the position of the cycle slip, which simplifies the correction process for the reason that no further judgment is required for cycle slip direction.

For brevity, the reminder of this paper is organized as follows. In Section II, the mathematical model of the atmospheric turbulence channel is furnished, as well as the receiver model of the coherent WOC system. In Section III, we discuss the calculation process and the PDF of discriminant parameters in the CSSC-CPE algorithm, and then the issue of optimal thresholds is determined. Section IV includes Monte-Carlo simulation results and analyses of the cycle slip probability and the symbol error rate (SER). Section V introduces the construction of the indoor experimental system and analyzes the experimental results. The conclusions are drawn in the last section.

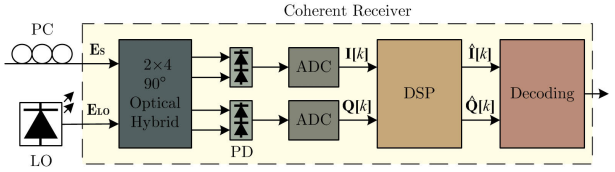

FIGURE 1. System structure of digital receiver in coherent optical communication.

II. SYSTEM MODEL

A. CHANNEL MODEL

For the coherent WOC system, uneven atmospheric temperature and pressure will result in atmospheric turbulence, thereby causing flux irradiance on the receiver plane to fluctuate randomly with time and space. The most common channel model to describe atmospheric turbulence is the log-normal distribution model [19]. The PDF of the received irradiance I under weak fluctuations can be expressed as follows

$$p_I(I) = \frac{1}{I\sigma_R\sqrt{2\pi}} \exp\left\{-\frac{1}{2\sigma_R{}^2}\left[\ln\left(\frac{I}{I_0}\right) + 0.5\sigma_R{}^2\right]^2\right\}, \tag{1}$$

where I_0 is the flux irradiance in the case of no atmospheric turbulence; $\sigma_R{}^2 = 1.23C_n^2\kappa^{7/6}z^{11/6}$ denotes the Rytov variance under the Kolmogorov turbulence theory [20]; C_n^2 is the atmospheric structure constant; $\kappa = 2\pi/\lambda$ represents the wave number; z means the link length.

Atmospheric turbulence can also lead to the random fluctuation of atmospheric refractivity, thereby causing random optical phase deviation. The deviation can be represented as a zero-mean Gaussian variable whose variance is presented in terms of J Zernike polynomials $\sigma_\phi^2 = C_J\left(\frac{D}{r_0}\right)^{5/3}$ [21], [22], where D stands for the aperture diameter and r_0 is the coherence diameter, describing the spatial correlation between phase fluctuations on the receiver plane. The coefficient C_J is equal to 1.0299 when no modal compensation is performed for terms correction at the receiver [23]. In the light of the Kolmogorov turbulence theory, the coherence diameter of plane waves is $r_0 = 1.68\left(C_n^2\kappa^2 z\right)^{-3/5}$ [24]. Considering that the aperture diameter is far smaller than the coherence diameter ($D \ll r_0$), beams on the receiver plane are spatially coherent at a single moment.

B. RECEIVER THEORY

For the single-polarization QPSK coherent WOC system, as shown in Fig. 1, signals received through atmospheric channels are firstly combined with local oscillator beams in a 2×4 90° optical hybrid. After that, photoelectric conversion is performed on the mixed signals by using two pairs of balanced detectors. For conceptional clarity, the positive integer

k represents the k^{th} symbol. Then, in-phase and quadrature components of the photocurrents are sampled by high-speed ADCs and can be expressed as $I[k]$ and $Q[k]$ respectively in (2). $\hat{I}[k]$ and $\hat{Q}[k]$ denotes their estimated values after DSP. To avoid redundancy, it needs to mention that every mathematical symbol with the indicia k means an arbitrary one in the whole manuscript.

$$\begin{aligned} I[k] &= RE_L E_S[k]\cos\left\{\theta_S[k]+\theta_{LW}[k]+\theta_\phi[k]\right\}+n_I[k] \\ Q[k] &= RE_L E_S[k]\sin\left\{\theta_S[k]+\theta_{LW}[k]+\theta_\phi[k]\right\}+n_Q[k] \end{aligned} \tag{2}$$

where R represents the responsivity of the photodiode and E_L stands for the amplitude of local oscillator beams. $E_S[k]$ and $\theta_S[k]$ denotes the amplitude and signal phase of the received signals, respectively, including log-normal fluctuations brought by atmospheric channels. $\theta_{LW}[k]$ is the phase noise arising from the transmission and local oscillator laser linewidths. And $\theta_{LW}[k]$ can be generally modeled as a Wiener process $\theta_{LW}[k] = \theta_{LW}[k-1] + w[k]$ where the increment $w[k]$ is an independent Gaussian variable with zero mean and variance $\sigma_{LW}{}^2 = 4\pi\Delta\nu T$ ($\Delta\nu$ and T represent laser linewidth and symbol period separately, assuming that the transmitter and receiver lasers have the same linewidth) [25]. $\theta_\phi[k]$ is the Gaussian phase fluctuation caused by atmospheric turbulence. $n[k]$ stands for the compound additive white Gaussian noise generated by the receivers, such as amplified spontaneous emission (ASE) noise, shot noise and thermal noise.

The sampled symbols are first normalized and I/Q balanced in the DSP, then after clock recovery and CFO correction, the phase information will eventually be recovered by the CPE with randomly occurring cycle slips. The cycle slips will cause phase offset as described in (4) of Section III-A. The proposed CSSS-CPE algorithm will be utilized to solve this problem, which will be depicted in Section III.

III. PRINCIPLES

A. THE STRUCTURE OF CSSC-CPE ALGORITHM

The k^{th} input symbol of the CSSC-CPE can be represented as $r[k] = \exp\{i[\theta_S[k]+\theta_N[k]]\}$, where the phase noise $\theta_N[k]$ considers the combined influences of the laser linewidth, atmospheric turbulence and receivers. Without loss of generality, other signal damages are assumed to be ignored or compensated, such as dispersion and nonlinearity, which are not the emphasis of this paper. Hence, the main obstacle is supposed to be $\theta_N[k]$, which will be estimated and compensated by the CSSC-CPE proposed in this paper. The CSSC-CPE consists of two cascaded stages, which are phase estimation stage and cycle slip correction stage. The flow chart is shown in Fig. 2.

The strategy of CSSC-CPE algorithm is depicted as follows. The phase noise $\theta_N[k]$ in $r[k]$ will be estimated through the VVPE algorithm at first, the phase noise estimate $x[k]$ is revealed as (3),

$$x[k] = \frac{1}{M} arg\left[\sum_{i=k-\lfloor(N-1)/2\rfloor}^{k+\lceil(N-1)/2\rceil} r^M[i]\right], \tag{3}$$

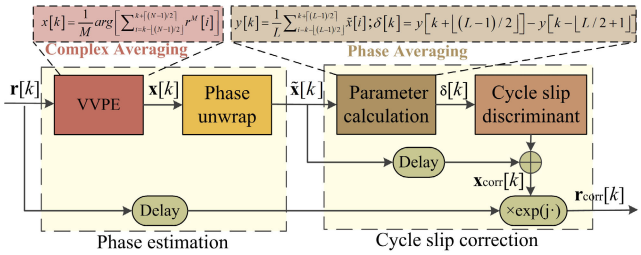

FIGURE 2. Flow chart of the CSSC-CPE algorithm.

where N and M represent the average length of the CPE and the modulation order separately, (for QPSK modulation $M = 4$). $\lceil\cdot\rceil$ and $\lfloor\cdot\rfloor$ denote the operations of rounding up and down to an integer. Besides, the operator $arg(\cdot)$ extracts its phase.

After dividing $x[k]$ by M, the phase noise could be equalized, which was enlarged to M times when removing the modulation information, but this operation also narrows the estimation range. In order to recover the phase wandering trajectory, the full-range estimate $\widetilde{x}[k]$ is deduced from a phase unwrapping progress performed on $x[k]$. And $\widetilde{x}[k]$ can be approximated as the true phase noise value $\theta_N[k]$ of the k^{th} symbol. However, due to the effects of residual phase noise, phase unwrapping can also cause cycle slips while extending the estimation range. In that case, $\widetilde{x}[k]$ will deviate from the true value $\theta_N[k]$ by $\pm\pi/2$ and therefore cause consecutive estimation errors, which is

$$\widetilde{x}[k] \approx \begin{cases} \theta_N[k], & \text{no CS at } k^{th} \text{ symbol} \\ \theta_N[k] \pm \dfrac{\pi}{2}, & \text{CS occured at } k^{th} \text{ symbol} \end{cases}. \tag{4}$$

The cycle slip correction stage will be utilized to solve this problem. Specifically, in parameter calculation step, $\widetilde{x}[k]$ is firstly processed by using the cumulative average method to obtain $y[k]$, which is

$$y[k] = \frac{1}{L}\sum_{i=k-\lfloor(L-1)/2\rfloor}^{k+\lceil(L-1)/2\rceil} \widetilde{x}[i] \ , \tag{5}$$

where L represents the cumulative length. Secondly, the average output is subtracted from the L-symbol delayed value to obtain the discriminant parameter $\delta[k]$, which is

$$\delta[k] = y[k+\lfloor(L-1)/2\rfloor] - y[k-\lfloor L/2+1\rfloor]. \tag{6}$$

Fig. 3 demonstrates the values of $\delta[k]$ under different conditions. The phase fluctuation caused by atmospheric turbulence and receivers in $\delta[k]$ could be well suppressed by two times average. And the laser phase noise is mitigated during the subtraction process due to its slowly varying characteristics. Therefore, the discriminant parameter $\delta[k]$ approaches 0 in the case of no cycle slip. With a cycle slip occurring, as shown by the two mutations of the green points near $k = 6000$ in Fig. 3, there will be a sudden positive or negative change of $\delta[k]$ according to the cycle slip direction, which indicates that the location and direction of cycle slips can be determined by setting thresholds. The confirmed cycle slips

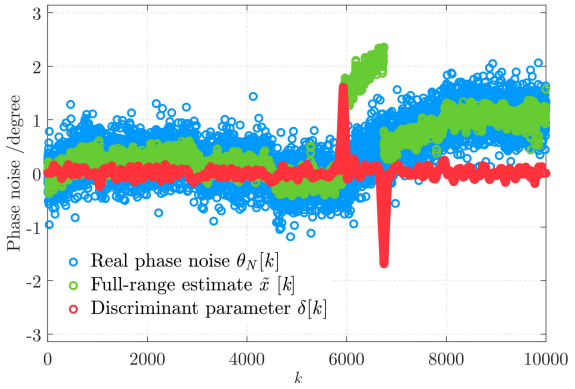

FIGURE 3. Variation trend of real phase noise $\theta_N[k]$, full-range estimate of phase noise with cycle slips $\tilde{x}[k]$ and discriminant parameter $\delta[k]$.

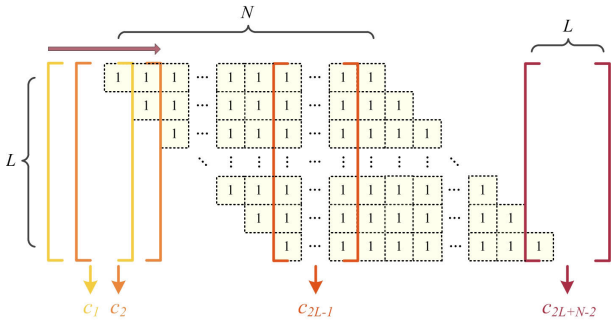

FIGURE 4. Method diagram for calculating coefficient $\{c_i\}$.

can be eliminated by adding the full-range estimate $\tilde{x}[k]$ and subsequent estimates with $\pi/2$ or $-\pi/2$. And the corrected phase information $r_{\text{corr}}[k]$ can be obtained by conjugate multiplication of the corrected estimate $x_{\text{corr}}[k]$ and $r[k]$.

B. THEORETICAL ANALYSIS AND OPTIMAL THRESHOLDS

The setting of thresholds has an important impact on cycle slip detection performance of CSSC-CPE. False judgment may occur when the thresholds are too low and cycle slips may be missed when the thresholds are too high. Assuming that no cycle slip occurs in the window centered on the k^{th} symbol (length of the window being $2L+N-1$), the output value $\delta[k]_{\text{noCS}}$ of CSSC-CPE can be expressed as

$$\delta[k]_{\text{noCS}} = \frac{1}{L}\sum_{i=k}^{k+L-1}\frac{1}{M}\arg\sum\nolimits_{j=i-\lfloor(N-1)/2\rfloor}^{i+\lceil(N-1)/2\rceil} r^M[j] - \frac{1}{L}\sum_{i=k-L}^{k-1}\frac{1}{M}\arg\sum\nolimits_{j=i-\lfloor(N-1)/2\rfloor}^{i+\lceil(N-1)/2\rceil} r^M[j]. \quad (7)$$

Lemma 1: For an arbitrary finite integer n and any integer p ($p = 1, 2, 3, \ldots, n$), it's assumed that $\{\alpha_p\}$ is a sequence of Wiener process, whose increment Δ_{p-1} obeys Gaussian distribution with zero mean and variance ${\sigma_W}^2$. Then the $\arg\sum_{p=1}^{n}\exp(i\alpha_p)$ can be approximately equal to $\frac{1}{n}\sum_{p=1}^{n}\alpha_p$ if ${\sigma_W}^2$ is far less than 1.

Proof: For keeping a logic consistency, the proof of the approximation is given in the Appendix. ■

In the light of Lemma 1. (7) can be further simplified as

$$\delta[k]_{\text{nocs}} \approx \frac{1}{MNL}\sum_{i=k}^{k+L-1}\sum_{j=i-\lfloor(N-1)/2\rfloor}^{i+\lceil(N-1)/2\rceil}\arg\left(r^M[j]\right) - \frac{1}{MNL}\sum_{i=k-L}^{k-1}\sum_{j=i-\lfloor(N-1)/2\rfloor}^{i+\lceil(N-1)/2\rceil}\arg\left(r^M[j]\right). \quad (8)$$

After removing the modulated data, it can be concluded that the phase noise caused by atmospheric turbulence and receivers can be well suppressed by the two average stages of CSSC-CPE. Therefore, the phase noise in $\delta[k]_{\text{noCS}}$ is mainly caused by the combined laser linewidth, so $\delta[k]_{\text{noCS}}$ can be derived in (9).

$$\delta[k]_{\text{noCS}} \approx \frac{1}{NL}\sum_{i=k-L-\lfloor(N-1)/2\rfloor}^{k+L-2+\lceil(N-1)/2\rceil} c_i\{\theta_{LW}[i+1]-\theta_{LW}[i]\} \quad (9)$$

where c_i represents the number of increments from the i^{th} symbol to the $(i+1)^{th}$ symbol in $\delta[k]_{\text{noCS}}$. The phase difference between any two adjacent symbols obeys zero-mean Gaussian random variables with variance ${\sigma_{LW}}^2 = 4\pi\Delta\nu T$, and then $\delta[k]_{\text{noCS}}$ can be expressed as

$$\delta[k]_{\text{noCS}} \sim N\left(0, 4\pi\frac{\sum_{i=k-L-\lfloor(N-1)/2\rfloor}^{k+L-2+\lceil(N-1)/2\rceil}{c_i}^2}{N^2L^2}\Delta\nu T\right). \quad (10)$$

It could be derived from (10) that the coefficients $\{c_i\}$ is the only barrier to overcome. Thus we propose a method to obtain the whole set $\{c_i\}$, thanks to a moving mask.

As shown in the Fig. 4, we can arrange the elements "1"s in N columns and L rows into an array, and start with the second row, aligning the first element of each row with the second element of the previous row.

The bracket in the same color could be assumed as a removable data mask. For an arbitrary integer i ranging from 1 to $2L+N-2$, c_i is equal to the output of the mask in location c_i by calculating the total number of elements "1". Both the length and height of the mask are L. The initial position of the mask lies in the first element on the leftmost side. The mask slides one column to the right every time until only one element on the rightmost side is included. After obtaining all the $2L+N-2$ outputs $\{c_i\}$, the probability density function $f_{\delta_k|\text{noCS}}$ of $\delta[k]_{\text{noCS}}$ can be calculated by (10).

Similarly, $f_{\delta_k|\text{CS}+}$ and $f_{\delta_k|\text{CS}-}$ could be derived, which represent the PDFs of positive slip $\delta[k]_{\text{CS}+}$ and negative slip $\delta[k]_{\text{CS}-}$ at symbol k, respectively. It needs to mention that the subscript "CS+" represents a positive cycle slip scenario, while the subscript "CS-" denotes that a negative cycle slip occurs. As can be seen from Fig. 5, the theoretical values well confirm with the results of 3×10^8 independent Monte Carlo simulations. This result can help to set thresholds more reasonably, and also verify the accuracy of the approximation adopted in Section III-B.

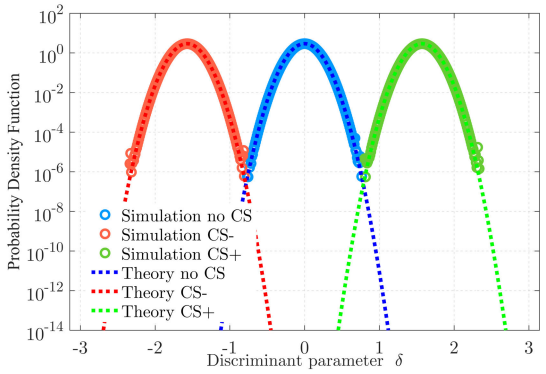

FIGURE 5. The probability density functions of $\delta[k]_{\mathrm{CS}-}$, $\delta[k]_{\mathrm{noCS}}$ and $\delta[k]_{\mathrm{CS}+}$, where the average lengths of phase estimation stage and cycle slip correction stage are $N = 55$ and $L = 50$, respectively. The laser linewidths are $\Delta v = 200$ kHz, and the symbol duration is $T_s = 5 \times 10^{-10}$ s.

The cycle slip probability after CSSC-CPE P_{CS} can be expressed as $P_{\mathrm{CS}} = \left(1 - P_{\mathrm{CS|CPE}}\right) \cdot P_{fal} + P_{\mathrm{CS|CPE}} \cdot (P_{mis} + P_{rev})$, where $P_{\mathrm{CS|CPE}}$ represents cycle slip probability after phase estimation stage; P_{fal} indicates the probability of false judgment in the case of no cycle slip; P_{mis} and P_{rev} stand for the probability of missing judgment and misjudgment of slip direction, respectively when a cycle slip occurs. P_{fal}, P_{mis} and P_{rev} are formulated in (11),

$$\begin{aligned} P_{fal} &= \int_{-\infty}^{-\delta_{th}} f_{\delta_k|\mathrm{noCS}}(\varepsilon)\, d\varepsilon + \int_{\delta_{th}}^{+\infty} f_{\delta_k|\mathrm{noCS}}(\varepsilon)\, d\varepsilon \\ P_{mis} &= \int_{-\delta_{th}}^{\delta_{th}} \left[f_{\delta_k|\mathrm{CS}-}(\varepsilon) + f_{\delta_k|\mathrm{CS}+}(\varepsilon)\right] d\varepsilon \\ P_{rev} &= \int_{-\infty}^{-\delta_{th}} f_{\delta_k|\mathrm{CS}+}(\varepsilon) d\varepsilon + \int_{\delta_{th}}^{+\infty} f_{\delta_k|\mathrm{CS}-}(\varepsilon) d\varepsilon. \end{aligned} \quad (11)$$

As shown in the left half of Fig. 6. The thresholds are established to lower the value of P_{CS}. The optimal positive and negative threshold $\pm\delta_{th}$ could be derived from the intersection points of $f_{\delta_k|\mathrm{CS}+}, f_{\delta_k|\mathrm{CS}-}$ and $f_{\delta_k|\mathrm{noCS}}$, which is

$$\delta_{th} = \pm\left[\frac{2\sigma^2}{\pi} \ln\left(\frac{1 - P_{\mathrm{CS|CPE}}}{P_{\mathrm{CS|CPE}}}\right) + \frac{2\sigma^2}{\pi} \ln 2 + \frac{\pi}{4}\right]. \quad (12)$$

where σ_δ^2 can be obtained by (10) through the known L, N and Δv, which is usually a value of order 10^{-3}. Take the forward cycle slip as an example, it's apparent that $P_{\mathrm{CS|CPE}} \ll 1 - P_{\mathrm{CS|CPE}} < 1$. The upper and lower bounds of δ_{th} could be derived in (13), with the help of the nature of false fractions, $\frac{1}{2P_{\mathrm{CS|CPE}}} < \frac{1-P_{\mathrm{CS|CPE}}}{P_{\mathrm{CS|CPE}}} < \frac{1}{P_{\mathrm{CS|CPE}}}$.

$$\begin{cases} \delta_{th}^{low} = \dfrac{2\sigma_\delta^2}{\pi} \ln\left(\dfrac{1}{2P_{\mathrm{CS|CPE}}}\right) + \dfrac{2\sigma_\delta^2}{\pi} \ln 2 + \dfrac{\pi}{4} \\ \delta_{th}^{up} = \dfrac{2\sigma_\delta^2}{\pi} \ln\left(\dfrac{1}{P_{\mathrm{CS|CPE}}}\right) + \dfrac{2\sigma_\delta^2}{\pi} \ln 2 + \dfrac{\pi}{4} \end{cases} \quad (13)$$

Taking $\delta_{th}^{up} - \delta_{th}^{low} = \frac{2\sigma_\delta^2}{\pi} \ln 2 \ll \frac{\pi}{4}$ into configuration, the bounds could be proved to be tight enough, so we use the upper bound δ_{th}^{up} for the approximation of δ_{th}. $P_{\mathrm{CS|CPE}}$ can be

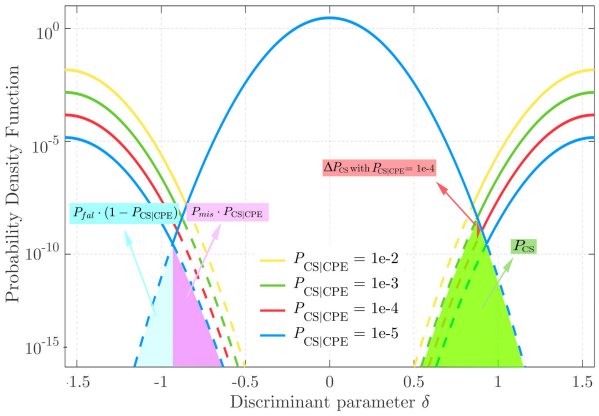

FIGURE 6. $f_{\delta_k|\mathrm{CS}+}$, $f_{\delta_k|\mathrm{CS}-}$, $f_{\delta_k|\mathrm{noCS}}$ versus discriminant parameter δ with different $P_{\mathrm{CS|CPE}}$ at $N = 55$, $L = 50$, $\Delta v = 200$ kHz, $T_s = 5 \times 10^{-10}$ s.

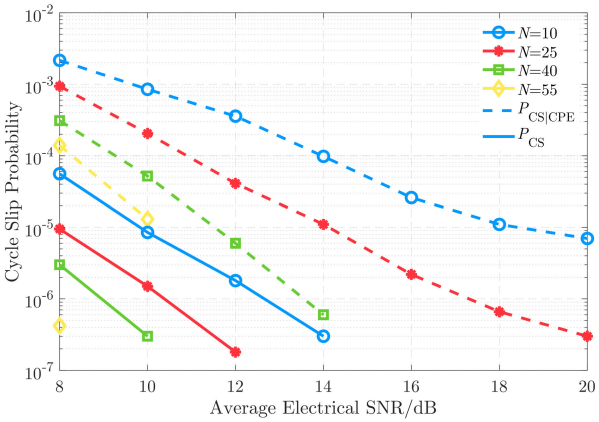

FIGURE 7. Cycle slip probability versus average electrical SNR before and after cycle slip correction stage.

represented as

$$P_{\mathrm{CS|CPE}} = \overline{P}_{\mathrm{CS|CPE}} \times \widetilde{P}_{\mathrm{CS|CPE}}. \quad (14)$$

where $\overline{P}_{\mathrm{CS|CPE}}$ represents the typical value of the cycle slip probability after phase estimation stage. $\widetilde{P}_{\mathrm{CS|CPE}}$ could be considered as the correction coefficient denoting the deviation between the actual cycle slip probability and the typical value. When $\overline{P}_{\mathrm{CS|CPE}} = 10^{-3}$, the deviation of the optimal threshold $\Delta\delta_{th}$ caused by $\widetilde{P}_{\mathrm{CS|CPE}}$ can be expressed as $\Delta\delta_{th} = -\frac{2\sigma_\delta^2}{\pi} \ln \widetilde{P}_{\mathrm{CS|CPE}}$. When the actual cycle slip probabilities are respectively 10^{-2}, 10^{-4}, 10^{-5}, that is, when $\widetilde{P}_{\mathrm{CS|CPE}}$ is respectively 10, 1/10, 1/100, the probability changes caused by can be expressed as

$$\begin{aligned} \Delta P_{\mathrm{CS}} = \int_{\delta_{th}}^{\delta_{th}+\Delta\delta_{th}} &\left[(1 - P_{\mathrm{CS|CPE}}) f_{\delta_k|\mathrm{noCS}}(\varepsilon)\right. \\ &\left. - 0.5 \times P_{\mathrm{CS|CPE}} f_{\delta_k|\mathrm{CS}+}(\varepsilon)\right] d\varepsilon. \end{aligned} \quad (15)$$

It's revealed that ΔP_{CS} stays with the magnitude of 10^{-8}, as also shown by the red shading in the right half of Fig. 6. The change of ΔP_{CS} caused by the difference of $P_{\mathrm{CS|CPE}}$ is small enough, so in the following simulation, under any condition of different σ_δ^2, the optimal threshold at $P_{\mathrm{CS|CPE}} = 10^{-3}$

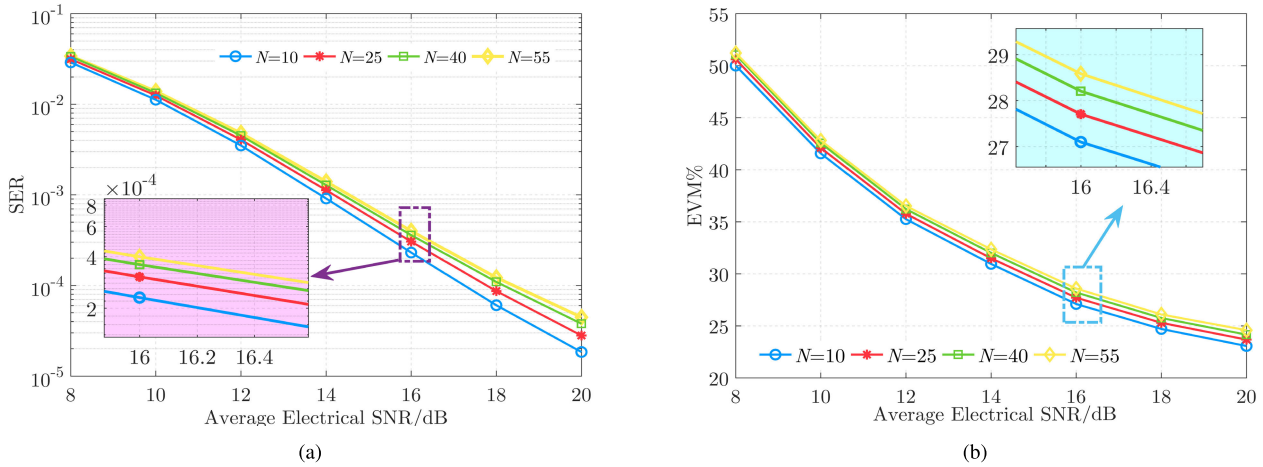

FIGURE 8. (a) SER and (b) EVM under different average electrical SNR conditions.

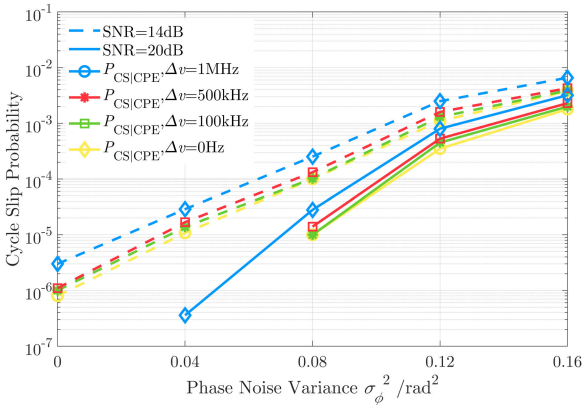

FIGURE 9. Cycle slip probability versus phase noise variance under different laser linewidths.

TABLE 1. Parameters used in the numerical simulation.

Parameters	Value
Wavelength λ	1550 nm
Propagation distance z	1 km
Atmospheric structure constant C_n^2	1.5×10^{-15} m$^{-2/3}$
Aperture diameter D	5 cm
Atmospheric coherent diameter r_0	24.5 cm
Log-amplitude variance σ_R^2	0.17
Phase noise variance σ_ϕ^2	0.07 rad^2
Laser linewidth Δv	100 kHz

could be considered as the universal threshold to identify cycle slips.

IV. SIMULATION RESULTS AND DISCUSSIONS

To verify the performance of the proposed algorithm, simulations are carried out on 100 M continuous single-polarization QPSK data with the symbol rate of 2 GBaud. The parameters are shown in Table 1.The cycle slips will be identified by a sliding SER calculation window of 200 symbols [18]. When the SER of the window is higher than 0.2, all the symbols after the middle of the window will be rotated with three other possible phases. If the SER after a certain rotation is significantly reduced, for example, less than 0.1, the result of the rotation will be considered as the actual phase estimate and one cycle slip will be counted. The whole data set will be processed by this method, and P_{CS} or $P_{CS|CPE}$ can be obtained by the ratio of the number of the cycle slips to the length of the symbol stream.

With the sampled symbols entering the DSP module, the proposed algorithm CSSC-CPE will be utilized for phase estimation and cycle slip correction. Fig. 7 compares the cycle slip probability after phase estimation stage $P_{CS|CPE}$ and after cycle slip correction stage P_{CS} under different average electrical SNRs and CPE average lengths. The average length in the cycle slip correction stage is $L = 50$. It is manifest from the simulation results that $P_{CS|CPE}$ can be reduced by enhancing SNR or increasing CPE average length N. When N is longer than 40, the CSSC-CPE can reduce the cycle slip probability by more than two orders of magnitude and completely eliminate cycle slips when the SNR is higher than 10 dB. When N is shorter than 25, the cycle slip after CPE stage can no longer be completely eliminated by improving the SNR. However, when the SNR is higher than 14 dB, the CSSC-CPE can still realize the detection and correction of all cycle slips, and even when the SNR is as low as 8 dB, CSSC-CPE can reduce the cycle slip probability P_{CS} to less than 10^{-4}, which satisfies the requirement of turbo differential decoding [15].

The cycle slip probability can be reduced by extending the CPE average length, however, the phase tracking capability will be weakened in that case, thereby increasing phase deviations and SERs [10], [11], [26]. For this reason, we compared the noise estimation performance of the CPE with different average lengths when the cycle slips are completely corrected. Fig. 8a and Fig. 8b respectively demonstrate the influences of the CPE average length N on SER and error vector magnitude (EVM) under different average electrical SNRs. It is found that the SER increases with the increase in N under the same SNR. When the SNR is 20 dB, the SER of CPE with $N = 10$ is only 41.26% of that with $N = 55$.

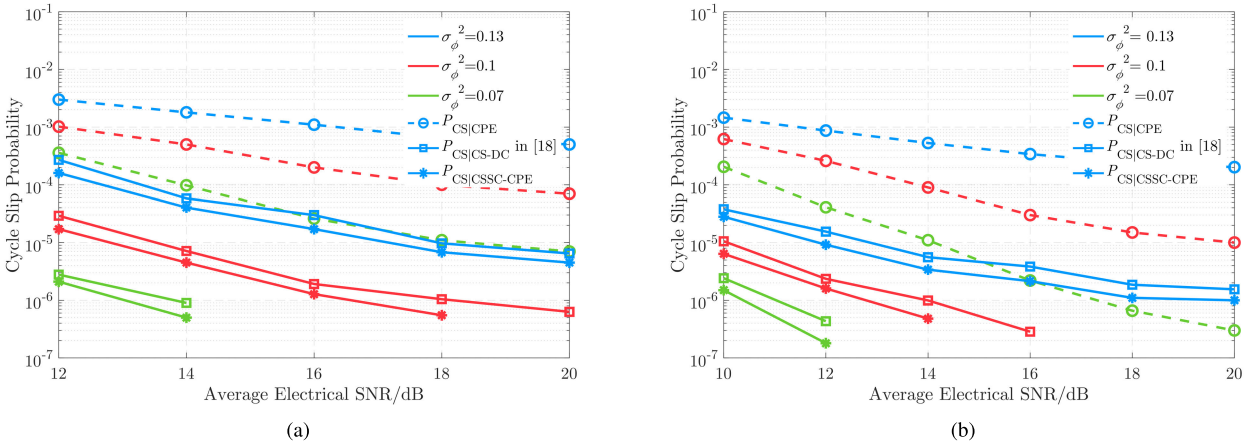

FIGURE 10. The relationship between the cycle slip probability and the average electrical SNR before and after the cycle slip correction with CSSC-CPE or CS-DC in [18]. The average length of phase estimation is (a) $N = 10$ and (b) $N = 25$ respectively.

Another performance measure for advanced modulation formats, EVM [27], also demonstrates that CPE estimates more accurately in shorter average lengths. Moreover, the cycle slip probability after CPE $P_{CS|CPE}$ will be greater when the CPE average length is shorter, which can validate the performance of the CSSC-CPE algorithm more effectively. Thus, in the subsequent analysis, we mainly analyze the cycle slip correction ability of the proposed algorithm under $N = 10$ and $N = 25$ separately.

In addition to the CPE average length, the cycle slip probability after CPE $P_{CS|CPE}$ is also related to the laser linewidth and the turbulence intensity. Fig. 9 shows the effect of different laser linewidths on the $P_{CS|CPE}$ under different atmospheric turbulence intensities. The CPE average length in the simulation is $N = 10$. As can be seen from the figure, whether the average electrical SNR is 14 dB or 20 dB, the cycle slip probability will increase as the laser linewidth becomes larger. However, in the case where the laser linewidth is less than 500 kHz, the rise in the $P_{CS|CPE}$ is not significant. In contrast, the increase in atmospheric turbulence intensity will evidently higher the probability of cycle slip, so we can consider that the atmospheric turbulence has a greater impact on the probability of cycle slip in the actual situation.

In order to verify the ability of the proposed CSSC-CPE to detect cycle slips under diverse turbulence intensities, simulations are carried out under different ${\sigma_\phi}^2$. In the simulation, another cycle slip correction algorithm CS-DC proposed by Ref. [18] is compared, which also needs no data assistance and uses the discriminant parameters to determine the slip position. The average length of the cycle slip correction stage of both algorithms is 50. In Fig. 10, the dotted line indicates the cycle slip probability before correction, and the cycle slip probability after correction by CS-DC or CSSC-CPE is represented by a solid line containing squares or stars, respectively. It can be concluded from the results that under the premise of the same $P_{CS|CPE}$, when the average length of CPE N is 10, the P_{CS} corrected by CSSC-CPE is 67.21% of that corrected by CS-DC. The ratio drops to 63.35% in the case of $N = 25$. The above phenomena indicate that the CSSC-CPE can more effectively eliminate cycle slips in atmospheric channel, which is mainly due to the fact that the short-time subtraction and two times average in CSSC-CPE can well suppress the phase noise caused by laser linewidth and atmospheric turbulence.

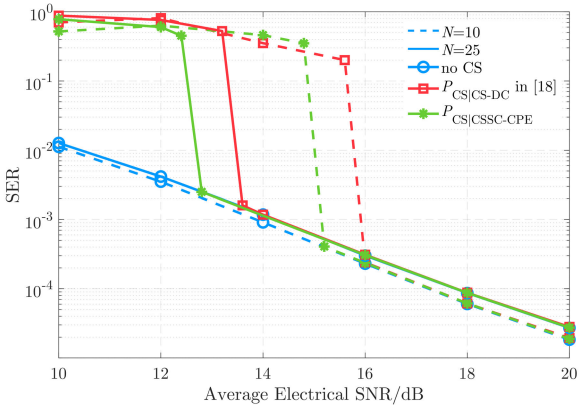

FIGURE 11. The relationship between SER and average electrical SNR after cycle slips are corrected by CS-DC in [18] or CSSC-CPE with ${\sigma_\phi}^2 = 0.07$.

Furthermore, we evaluated the SER of the system under different average electrical SNRs after cycle slips are corrected by the two algorithms. The parameters are set in the same way as in Fig. 10. It can be seen from Fig. 11, with a satisfying SNR, both algorithms can make the processed SER almost reach the degree of no cycle slip occurrence, which means that both algorithms can accurately find the position where the cycle slip occurs. But it's worth noting that when the average length of the CPE stage is 10 or 25, compared with CS-DC, the SNR requirement of CSSC-CPE can be reduced by 0.6 dB when the cycle slip can be completely eliminated. Therefore, the CSSC-CPE can be considered to be more advantageous for coherent WOC systems.

Then we simulated the cycle slip probability after CSSC-CPE P_{CS} of different average lengths in the cycle

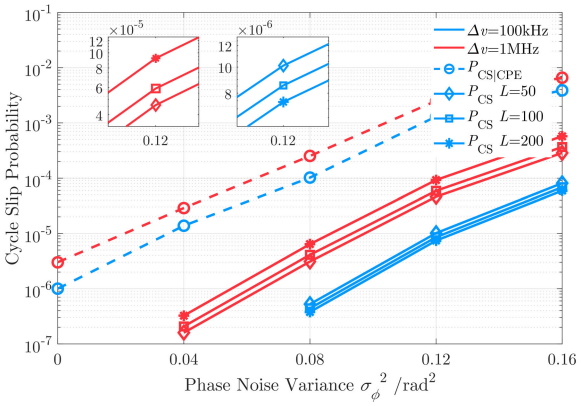

FIGURE 12. Cycle slip probability versus phase noise variance under different average lengths.

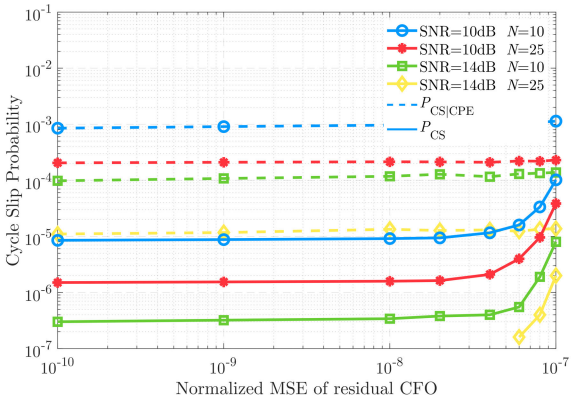

FIGURE 13. Cycle slip probability versus normalized MSE of residual CFO before and after cycle slip correction.

TABLE 2. Complexity comparison of two algorithms in calculating discrimination parameters.

Algorithm	Real multipliers	Real adders	Comparators
CS-DC in [18]	$4L+2$	$4L-1$	1
Proposed	0	$2L-1$	2

slip correction stage L under different atmospheric turbulence intensities. The average length of the CPE stage in the simulation is $N = 10$, and the average electrical SNR is 14 dB. As can be seen from Fig. 12, when the linewidth of the laser is 100 kHz, P_{CS} decreases slightly with the increase of L. However, when the linewidth of the laser is as high as 1 MHz, the rise of L causes an increase in P_{CS}. This is because as the average length increases, the correlation between the two average segments is weaker. When the laser linewidth is large, the phase noise caused by the laser linewidth in the discriminant parameter cannot be well offset by the difference between the two segments.

For the coherent WOC system, the CFO correction needs to be performed before phase estimation. In the actual system, however, CFO usually cannot be completely corrected. The phase noise caused by residual CFO will affect the performance of CSSC-CPE. Therefore, it is necessary to study the CFO tolerance of the proposed algorithm. Fig. 13 shows the relations between cycle slip probability the normalized mean square error (MSE, defined as $E\left[|\Delta f \cdot T_s|^2\right]$) of residue CFO. The simulation considers the influences of the average electrical SNR and the average length N in CPE. It can be seen from Fig. 13 that no matter $N = 10$ or $N = 25$, there is almost no influence on $P_{CS|CPE}$ or P_{CS} when the MSE is less than 4×10^{-8}. Considering that the MSE of the residual CFO of the commonly used CFO correction algorithm can reach 10^{-10} or less [28], it is safe to conclude that the CSSC-CPE has sufficient residual CFO tolerance.

Finally, we compared the complexity of two non-data-aided cycle slip correction algorithms. Since the phase estimation and the phase unwrapping are the common premise of cycle slip correction algorithms with the same complexity, it makes more sense to analyze the number of computations required to obtain the discriminant parameters. Compared with CS-DC in Ref. [18], the proposed algorithm omits some adders and multipliers because it contains only a simple cumulative averaging process of angle values and has no steps of square or modulus for complex variables. However, since the discriminant parameters obtained from each calculation need to be compared with two thresholds, the proposed algorithm needs an additional comparator. Table 2 lists the complexity comparisons between the two algorithms, where L represents the cumulative length in calculating the discriminant parameters.

V. EXPERIMENTAL RESULTS

In order to verify the performance of the CSSC-CPE in the practical WOC system, indoor experiments were performed. Fig. 14a and Fig. 14b respectively show the structural block diagram and scene of the experimental system. In the experiment, a 1550 nm precise tunable laser source is used at the transmitter, the wavelength tuning accuracy is 10 pm and the linewidth is less than 10 kHz. The laser can be precisely adjusted to maintain the same frequency as the local oscillator laser at the receiver. The 4 Gbps rate data sequence is first generated by the arbitrary waveform generator (AWG) and then amplified by the driver amplifier to a certain electrical level (5 V). The laser will be modulated by the data sequence in a two-channel Mach-Zehnder modulator (MZM) and entered into the WOC system by the transmitting antenna.

In the WOC link, we use a laboratory turbulence generator to simulate the actual atmospheric environment. The laboratory turbulence generator is a partially sealed box with two glass plates at each side that allows optical signals to propagate inside. The temperature and the air velocity in the box can be adjusted by the internal heating device and the top connected blower to simulate atmospheric turbulence.

The laser beam will be collected by another antenna at the receiver and coupled into the fiber link. Then the optical signal will beat with 1550 nm local oscillator in a 2×4 90° optical hybrid, and the output signals will be detected by two high-speed balance photodetectors with 40 GHz bandwidth. The data acquisition unit will be implemented by a 100 GS/s

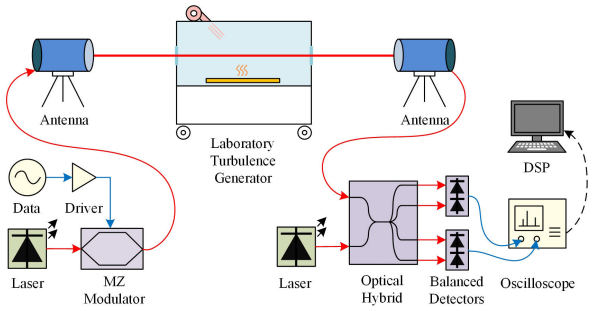

(a)

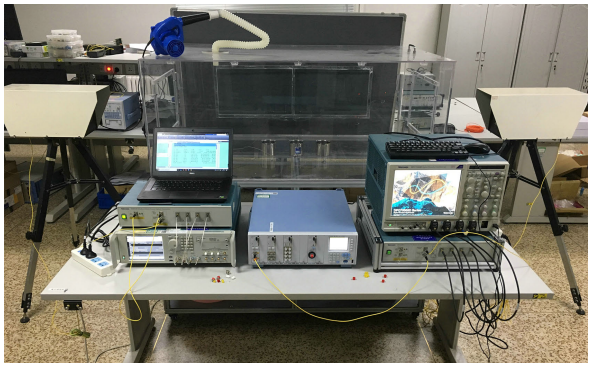

(b)

FIGURE 14. (a) Block diagram and (b) photograph of the experimental setup.

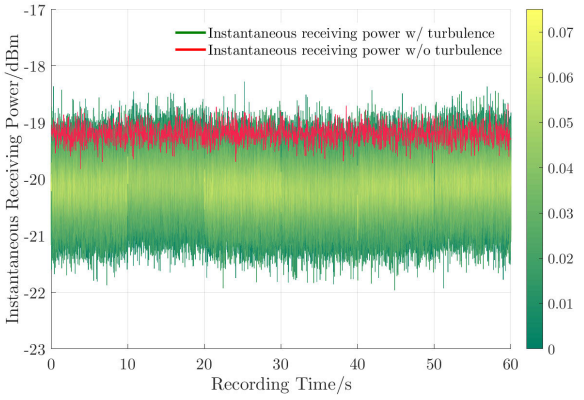

FIGURE 15. Instantaneous power recorded by the receiver.

high-speed oscilloscope with a bandwidth of 33 GHz. The sampled data will be displayed on the oscilloscope and sent to the computer for subsequent digital signal processing.

In the experiment, the instantaneous receiving power is measured first. Fig. 15 shows the optical power changes received in one minute with and without turbulence when the transmitted power is −5 dBm. It can be seen from the red line in the figure that the instantaneous receiving power is about -19 dBm when no turbulence is introduced, which means that the path loss of the entire optical link is about 14 dB. The curve represented by the yellow-green gradient color indicates that the turbulence generated by the laboratory turbulence generator causes fluctuations in light intensity. A piecewise probability density analysis of instantaneous receiving power is also carried out, and the

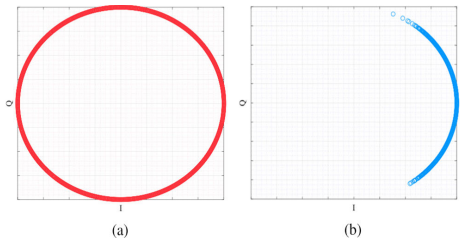

(a) (b)

FIGURE 16. The estimated phase noise (a) before and (b) after CSSC-CPE's cycle slip correction stage.

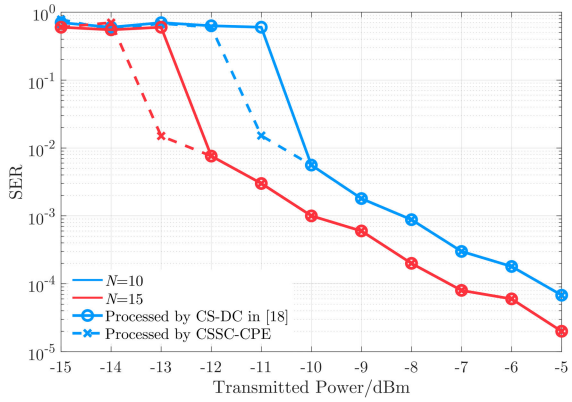

FIGURE 17. The symbol error rate of two cycle slip correction algorithms under different transmitted power.

probability at a certain power is expressed by the background color. It can be considered that the received intensity through turbulence is approximately obeys log-normal distribution, and the subsequent experiments will be performed in the same environment.

Fig. 16a and Fig. 16b respectively show the constellation of the estimated phase noise before and after the cycle slip correction stage of the CSSC-CPE. It can be seen that the constellation points in the Fig. 16b converge near the zero phase. That is to say, the cycle slip that causes the estimated phase noise to shift by an integer multiple of $\pi/2$ can be effectively eliminated by the algorithm.

The symbol error rate after two kinds of non-data-aided cycle slip correction algorithms are compared with different transmitted power. As can be seen from Fig. 17, when the cycle slip can be completely corrected, the CSSC-CPE has a lower minimum optical power requirement relative to the CS-DC no matter $N = 10$ or $N = 25$. The experimental results are basically consistent with the simulation curves in Fig. 11, and the results also demonstrate the feasibility and effectiveness of the CSSC-CPE in WOC system.

VI. CONCLUSION

This paper proposes an improved phase estimation algorithm CSSC-CPE for coherent WOC systems, which can detect and correct the cycle slips generated in the CPE process by the discriminant parameter δ without data assistance. The PDF of δ is systematically deduced and the optimal thresholds are determined. In addition, numerical simulations are carried out under weak turbulence condition. The results show that the

$$
\begin{aligned}
L &= \arg\sum_{p=1}^{n}\exp(ia_p) = \frac{\sum_{p=1}^{n}\sin a_p}{\sum_{p=1}^{n}\cos a_p} \\
&= \frac{\sin\alpha_1 + \sum_{p=1}^{n-1}\sin\left(\alpha_1 + \sum_{l=1}^{p}\Delta_l\right)}{\cos\alpha_1 + \sum_{p=1}^{n-1}\cos\left(\alpha_1 + \sum_{l=1}^{p}\Delta_l\right)} \\
&= \frac{\sin\alpha_1\left[1 + \sum_{p=1}^{n-1}\cos\left(\sum_{l=1}^{p}\Delta_l\right)\right] + \cos\alpha_1\left[\sum_{p=1}^{n-1}\sin\left(\sum_{l=1}^{p}\Delta_l\right)\right]}{\cos\alpha_1\left[1 + \sum_{p=1}^{n-1}\cos\left(\sum_{l=1}^{p}\Delta_l\right)\right] - \sin\alpha_1\left[\sum_{p=1}^{n-1}\sin\left(\sum_{l=1}^{p}\Delta_l\right)\right]}
\end{aligned} \tag{A3}
$$

CSSC-CPE can efficaciously reduce the cycle slip probability about two orders of magnitude in low SNR scenarios and completely eliminate cycle slips when the SNR is greater than 14 dB. Meanwhile, when the average length N of CPE is 10, CSSC-CPE can lessen the cycle slip probability to 67.21% compared with the related algorithm, and reduce the SNR requirement of eliminating the cycle slip completely by 0.6 dB. These performances will also increase as N becomes larger. Hence, after the indoor experiment verification, we have reason to believe that CSSC-CPE can be applied to coherent WOC systems and provide a novel approach to deal with cycle slip problems.

APPENDIX

In this appendix, the proof and explanation of Lemma 1 are depicted. The approximation to be prove can be given in (A1).

$$
\arg\sum_{p=1}^{n}\exp(i\alpha_p) \approx \frac{1}{n}\sum_{p=1}^{n}\alpha_p. \tag{A1}
$$

At first, efforts are made to simplify the left side of (A1). For any integer p ranging from 1 to n, all the α_ps are demonstrated as (A2)

$$
\begin{aligned}
&\alpha_1 = \alpha_1; \\
&\alpha_2 = \alpha_1 + \Delta_1; \\
&\alpha_3 = \alpha_1 + \Delta_1 + \Delta_2; \\
&\vdots \\
&\alpha_n = \alpha_1 + \Delta_1 + \Delta_2 + \ldots + \Delta_{n-1};
\end{aligned} \tag{A2}
$$

With the help of (A2), the left side of (A1) becomes (A3), as shown at the top of this page, where L denotes the left side of (A1).

After using $\alpha = \tan\left[\tan^{-1}(\alpha)\right]$ and some derivation, (A4) could be derived.

$$
\begin{aligned}
L &= \frac{\tan\alpha_1 + \dfrac{\sum_{p=1}^{n-1}\sin\left(\sum_{l=1}^{p}\Delta_l\right)}{1 + \sum_{p=1}^{n-1}\cos\left(\sum_{l=1}^{p}\Delta_l\right)}}{1 - \tan\alpha_1\left[\dfrac{\sum_{p=1}^{n-1}\sin\left(\sum_{l=1}^{p}\Delta_l\right)}{1 + \sum_{p=1}^{n-1}\cos\left(\sum_{l=1}^{p}\Delta_l\right)}\right]} \\
&= \tan\left(\alpha_1 + \arctan\frac{\sum_{p=1}^{n-1}\sin\left(\sum_{l=1}^{p}\Delta_l\right)}{1 + \sum_{p=1}^{n-1}\cos\left(\sum_{l=1}^{p}\Delta_l\right)}\right).
\end{aligned} \tag{A4}
$$

We assume R to be the right side of (A1), which is derived in (A5).

$$
\begin{aligned}
R &= \tan(\frac{\alpha_1 + \alpha_2 + \alpha_3 + \ldots + \alpha_n}{n}) \\
&= \tan\left(\alpha_1 + \frac{(n-1)\,\Delta_1}{n} + \frac{(n-2)\,\Delta_2}{n} + \ldots + \frac{\Delta_{n-1}}{n}\right).
\end{aligned} \tag{A5}
$$

By comparing (A4) and (A5), all what we need to prove is the approximation, which is

$$
\begin{aligned}
&\tan^{-1}\frac{\sum_{p=1}^{n-1}\sin\left(\sum_{l=1}^{p}\Delta_l\right)}{1 + \sum_{p=1}^{n-1}\cos\left(\sum_{l=1}^{p}\Delta_l\right)} \\
&\quad\approx \frac{(n-1)\,\Delta_1}{n} + \frac{(n-2)\,\Delta_2}{n} + \ldots + \frac{\Delta_{n-1}}{n}.
\end{aligned} \tag{A6}
$$

To the best of the authors' knowledge, (A6) is still too sophisticated to be proven. But it's noted that the left side of (A6) could be reformulated as

$$
\tan^{-1}\left[\frac{(n-1)\,\Delta_1}{n} + \frac{(n-2)\,\Delta_2}{n} + \ldots + \frac{\Delta_{n-1}}{n}\right],
$$

with the help of $\sin\Delta_p \approx \Delta_p$ and $\cos\Delta_p \approx 1$. That is to say, either side of (A6) is conceived to be equal to the other side when $\Delta_p \approx 0$.

Considering it's not a strict proof, the simulation method is utilized to testify (A6). Due to the Gaussian distribution with mean μ and variance σ^2, we could obtain $P\left\{\left|\Delta_p - \mu\right| < 3\sigma\right\} \approx 99.73\%$. When T takes 5×10^{-10} s and Δv takes a typical value of 10^5 Hz, we derive

$$
P\left\{-7.52 \times 10^{-2} < \Delta_p < 7.52 \times 10^{-2}\right\} \approx 99.73\%. \tag{A7}
$$

According to the PauTa criterion, we can remove exceptional data and approximate it as $\Delta_p \in (-7.52 \times 10^{-2}, 7.52 \times 10^{-2})$. In this range, we get the probability of error value of the following formula by 10^8 independent Monte Carlo simulations. ξ is defined as the normalized difference between the left side and right side of (A6), which is given as

$$
\xi = \frac{\tan^{-1}\frac{\sum_{p=1}^{n-1}\sin\left(\sum_{l=1}^{p}\Delta_l\right)}{1+\sum_{p=1}^{n-1}\cos\left(\sum_{l=1}^{p}\Delta_l\right)} - \frac{(n-1)\Delta_1}{n} + \ldots + \frac{\Delta_{n-1}}{n}}{\frac{(n-1)\Delta_1}{n} + \ldots + \frac{\Delta_{n-1}}{n}} \tag{A8}
$$

The computation results of ξ are listed in shown in Table A1. It could be concluded that the left and right sides of (A1) can be approximately equal by simulation.

TABLE A1. Probability of error range ξ.

Scope of ξ	$\geq 0.1\%$	$\geq 0.05\%$	$\geq 0.01\%$
Probability	3.23×10^{-6}	5.69×10^{-6}	2.47×10^{-5}

REFERENCES

[1] M. A. Khalighi and M. Uysal, "Survey on free space optical communication: A communication theory perspective," *IEEE Commun. Surveys Tuts.*, vol. 16, no. 4, pp. 2231–2258, Nov. 2014.

[2] A. Belmonte and J. M. Kahn, "Capacity of coherent free-space optical links using atmospheric compensation techniques," *Opt. Express*, vol. 17, no. 4, pp. 2763–2773, Feb. 2009.

[3] A. P. T. Lau, Y. Gao, Q. Sui, D. Wang, Q. Zhuge, M. H. Morsy-Osman, M. Chagnon, X. Xu, C. Lu, and D. V. Plant, "Advanced DSP techniques enabling high spectral efficiency and flexible transmissions: Toward elastic optical networks," *IEEE Signal Process. Mag.*, vol. 31, no. 2, pp. 82–92, Mar. 2017.

[4] S. J. Savory, "Digital coherent optical receivers: Algorithms and subsystems," *IEEE J. Sel. Topics Quantum Electron.*, vol. 16, no. 5, pp. 1164–1179, Sep. 2010.

[5] M. Kuschnerov, F. N. Hauske, K. Piyawanno, B. Spinnler, M. S. Alfiad, A. Napoli, and B. Lankl, "DSP for Coherent Single-Carrier Receivers," *J. Lightw. Technol.*, vol. 27, no. 16, pp. 3614–3622, Aug. 15, 2009.

[6] M. S. Faruk and S. J. Savory, "Digital signal processing for coherent transceivers employing multilevel formats," *J. Lightw. Technol.*, vol. 35, no. 5, pp. 1125–1141, Mar. 1, 2017.

[7] X. Zhou, "Efficient clock and carrier recovery algorithms for single-carrier coherent optical systems: A systematic review on challenges and recent progress," *IEEE Signal Process. Mag.*, vol. 31, no. 2, pp. 35–45, Mar. 2014.

[8] X. Li, T. Geng, S. Ma, Y. Li, S. Gao, and Z. Wu, "Performance improvement of coherent free-space optical communication with quadrature phase-shift keying modulation using digital phase estimation," *Appl. Opt.*, vol. 56, no. 16, pp. 4695–4701, May 2017.

[9] V. Rozental, D. Kong, B. Corcoran, D. Mello, and A. J. Lowery, "Filtered carrier phase estimator for high-order QAM optical systems," *J. Lightw. Technol.*, vol. 36, no. 14, pp. 2980–2993, Jul. 15, 2018.

[10] C. Fludger, D. Nuss, and T. Kupfer, "Cycle-slips in 100G DP-QPSK transmission systems," presented at the Opt. Fiber Commun. Conf., 2012. doi: 10.1364/OFC.2012.OTu2G.1.

[11] A. Bisplinghoff, C. Vogel, T. Kupfer, S. Langenbach, and B. Schmauss, "Slip-reduced carrier phase estimation for coherent transmission in the presence of non-linear phase noise," presented at the Opt. Fiber Commun. Conf., 2013. doi: 10.1364/OFC.2013.OTu3I.1.

[12] M. Qiu, Q. Zhuge, M. Chagnon, F. Zhang, and D. V. Plant, "Laser phase noise effects and joint carrier phase recovery in coherent optical transmissions with digital subcarrier multiplexing," *IEEE Photon. J.*, vol. 9, no. 1, Feb. 2017, Art. no. 7901013.

[13] V. N. Rozental, D. Kong, B. Foo, B. Corcoran, and A. J. Lowery, "Cycle-slip-less low-complexity phase recovery algorithm for coherent optical receivers," *Opt. Lett.*, vol. 42, no. 18, pp. 3554–3557, Sep. 2017.

[14] T. Mizuochi, Y. Miyata, K. Kubo, T. Sugihara, K. Onohara, and H. Yoshida, "Progress in soft-decision FEC," presented at the Opt. Fiber Commun. Conf., 2011. doi: 10.1364/NFOEC.2011.NWC2.

[15] F. Yu, N. Stojanovic, F. N. Hauske, D. Chang, Z. Xiao, G. Bauch, D. Pflueger, C. Xie, Y. Zhao, L. Jin, Y. Li, L. Li, X. Xu, and Q. Xiong, "Soft-decision LDPC turbo decoding for DQPSK modulation in coherent optical receivers," presented at the European Conf. on Optical Comm., 2011. doi: 10.1364/ECOC.2011.We.10.P1.70.

[16] H. Cheng, Y. Li, F. Zhang, J. Wu, J. Lu, G. Zhang, J. Xu, and J. Lin, "Pilot-symbols-aided cycle slip mitigation for DP-16QAM optical communication systems," *Opt. Express*, vol. 21, no. 19, pp. 22166–22172, Sep. 2013.

[17] H. Cheng, Y. Li, D. Kong, J. Zang, J. Wu, and J. Lin, "Low overhead slipless carrier phase estimation scheme," *Opt. Express*, vol. 22, no. 17, pp. 20740–20747, Aug. 2014.

[18] Y. Gao, E. Ha, A. P. T. Lau, C. Lu, X. Xu, and L. Li, "Non-data-aided and universal cycle slip detection and correction for coherent communication systems," *Opt. Express*, vol. 22, no. 25, pp. 31167–31179, Dec. 2014.

[19] A. K. Majumdar and J. C. Ricklin, *Free-Space Laser Communications*. New York, NY, USA: Springer, 2008.

[20] L. C. Andrews and R. L. Phillips, *Laser Beam Propagation Through Random Media*, 2nd ed. Washington, DC, USA: SPIE, 2005.

[21] A. Belmonte and J. M. Kahn, "Performance of synchronous optical receivers using atmospheric compensation techniques," *Opt. Express*, vol. 16, no. 18, pp. 14151–14162, Sep. 2008.

[22] R. J. Noll, "Zernike polynomials and atmospheric turbulence," *J. Opt. Soc. Amer.*, vol. 66, no. 3, pp. 207–211, 1976.

[23] A. Belmonte and J. M. Khan, "Capacity of coherent free-space optical links using diversity-combining techniques," *Opt. Express*, vol. 17, no. 15, pp. 12601–12611, Jul. 2009.

[24] D. L. Fried, "Optical heterodyne detection of an atmospherically distorted signal wave front," *Proc. IEEE*, vol. 55, no. 1, pp. 57–77, Jan. 1967.

[25] D. Ly-Gagnon, S. Tsukamoto, K. Katoh, and K. Kikuchi, "Coherent detection of optical quadrature phase-shift keying signals with carrier phase estimation," *J. Lightw. Technol.*, vol. 24, no. 1, pp. 12–21, Jan. 2006.

[26] G. Goldfarb and G. Li, "BER estimation of QPSK homodyne detection with carrier phase estimation using digital signal processing," *Opt. Express*, vol. 14, no. 18, pp. 8043–8053, Sep. 2006.

[27] R. Schmogrow, "Error vector magnitude as a performance measure for advanced modulation formats," *IEEE Photon. Technol. Lett.*, vol. 24, no. 1, pp. 61–63, Jan. 1, 2012.

[28] Y. Liu, Y. Peng, S. Wang, and Z. Chen, "Improved FFT-based frequency offset estimation algorithm for coherent optical systems," *IEEE Photon. Technol. Lett.*, vol. 26, no. 6, pp. 613–616, Mar. 15, 2014.

YE WANG received the B.S. degree in electronic science and technology from Northwest University (NWU), Xi'an, China, in 2014. He is currently pursuing the Ph.D. degree in circuits and systems with the University of Chinese Academy of Sciences (UCAS), Beijing, China. He is also a Trainee with the Changchun Institute of Optics, Fine Mechanics and Physics (CIOMP), Chinese Academy of Sciences. His research interests include coherent detection and digital signal processing.

ZHIYONG WU is currently a Full Researcher with the Changchun Institute of Optics, Fine Mechanics and Physics (CIOMP), Chinese Academy of Sciences, Changchun, China. His current research interests include free-space optics and fiber communication.

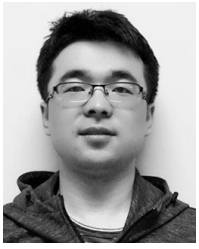

XUELIANG LI received the B.S. degree in optical information engineering from Jilin University (JLU), Changchun, China, in 2012, and the Ph.D. degree in electronic circuits and systems from the University of Chinese Academy of Sciences (UCAS), Beijing, China, in 2017. He is currently a Research Assistant with the Changchun Institute of Optics, Fine Mechanics and Physics (CIOMP), Chinese Academy of Sciences, Changchun. His current research interests include free-space optics and fiber communication.

TIANWEN GENG received the B.S. and M.S. degrees in electronic circuits and systems from Jilin University (JLU), Changchun, China, in 2004 and 2007, respectively. He is currently an Associate Researcher with the Changchun Institute of Optics, Fine Mechanics and Physics (CIOMP), Chinese Academy of Sciences, Changchun. His current research interests include free-space optics and fiber communication.

SHUANG MA received the B.S. degree in optical information engineering from Jilin University (JLU), Changchun, China, in 2010, and the Ph.D. degree in electronic circuits and systems from the University of Chinese Academy of Sciences (UCAS), Beijing, China, in 2016. He is currently a Research Assistant with the Changchun Institute of Optics, Fine Mechanics and Physics (CIOMP), Chinese Academy of Sciences, Changchun. His current research interests include free-space optics and fiber communication.

LIN LI received the B.S. degree in communication engineering from Shandong University (SDU), Weihai, China, in 2015. He is currently pursuing the Ph.D. degree in circuits and systems with the University of Chinese Academy of Sciences (UCAS), Beijing, China. He is also a Trainee with the Changchun Institute of Optics, Fine Mechanics and Physics (CIOMP), Chinese Academy of Sciences. His research interests include coherent detection and digital signal.

SHIJIE GAO received the B.S. degree in mechanical and electrical engineering from HUST, Harbin, China, in 2002, and the M.S. and Ph.D. degrees in electronic circuits and systems from the University of Chinese Academy of Sciences (UCAS), Beijing, China, in 2006 and 2015, respectively. He is currently an Associate Researcher with the Changchun Institute of Optics, Fine Mechanics and Physics (CIOMP), Chinese Academy of Sciences, Changchun, China. His current research interests include free-space optics and laser technology.

YATIAN LI received the B.S. and M.S. degrees (Hons.) in communications engineering from the Harbin Institute of Technology (HIT), Harbin, China, in 2013 and 2015, respectively. He is currently pursuing the Ph.D. degree in mechanical and electrical engineering with the University of Chinese Academy of Sciences (UCAS), Beijing, China. He is also a Research Assistant with the Laboratory of Laser Communication, Changchun Institute of Optics, Fine Mechanics and Physics (CIOMP), Chinese Academy of Sciences (CAS), Changchun, China. His research interests include free-space optics and wireless communications.